Grain Growth in Multiple Scales of Polycrystalline AZ31 Magnesium Alloy by Phase-Field Simulation

Y. WU, B.Y. ZONG, X.G. ZHANG, and M.T. WANG

A multiscale phase-field model was established on the assumption of an isotropic single-phase system to simulate the realistic spatiotemporal process of grain growth for polycrystalline Mg-Al-Zn alloy AZ31, especially to determine the mechanisms for unique nanostructure evolution. The expression of the local free energy density function was improved according to different driving forces. The grain boundary range and grain boundary energy were studied in each scale to determine the correct gradient and coupling parameters, respectively. It is shown that the grain boundary energy in nanoscales is lower down to about half that in the micron scale, the time exponent n in the kinetic equation is varied from 5 to 2 from the nanograins to the micrograins, and the grain growth rate in nanoscale is much slower in an order of magnitude than that in the micron scale. These findings can be proven by the limited experimental results in the literature. Simulations expose that the solute atoms like to segregate at the grain boundaries much more severely in nanostructure than that in conventional microstructure, and this may be the reason why nanostructure shows a low boundary mobility to result in a strange low grain growth rate at up to an initial long annealing time.

DOI: 10.1007/s11661-012-1478-9

I. INTRODUCTION

NANOCRYSTALLINE materials were first defined by Gleiter in 1981, who also presented ways to design them. Since then, the research about nanocrystalline materials and nanotechnology had been very active because of their unique physical and mechanical properties.[1–4] Certain experiments revealed that the measured properties of materials explicitly exhibited size dependence. For instance, the relationship of the strength and grain size followed the Hall–Petch relationship ($\sigma_s = \sigma_0 + Kd^{-1/2}$) for conventional polycrystalline materials, but it was not for the nanocrystalline materials, depending on nanostructure features.[1] The difficulties in experimental investigations are not only the huge cost but also the diversity of the measurements without physical models due to the different test conditions among so many individual researchers. With the advent of powerful modern material science, the multiscale simulation techniques in which either multiple time or multiple spatial scales are treated simultaneously may be the potential tool to deal with the complicated problem of microstructural evolution.[5,6]

Y. WU, Ph.D. Student, and B.Y. ZONG, Professor, are with the Key Laboratory for Anisotropy and Texture of Materials (Ministry of Education), Northeastern University, Shenyang 110004, People's Republic of China. Contact e-mail: zongyp@smm.neu.edu.cn X.G. ZHANG is Lecturer, Key Laboratory for Anisotropy and Texture of Materials (Ministry of Education), Northeastern University, and Department of Mathematics and Physics, Shenyang University of Chemical Technology, Shenyang 110142, People's Republic of China. M.T. WANG, Engineer, is with Shanxi Taigang Stainless Steel Company Limited, Taiyuan 030003, People's Republic of China.

Manuscript submitted June 6, 2012.
Article published online October 19, 2012

Multiscale computational methodology is an integration of many different computational methodologies, and it is an intermediate tool to bridge from angstroms to microns. Some authors thought the idea of multiscale modeling bridged the analytical and numerical models;[7] others thought it should be extended to build up bridges between microstructural simulation and property predictions, and between processing modeling and property predictions.[8] Reference 9 describes the development of the quasi-continuum method linking atomistic and continuum models through the finite element method. Reference 10 presents a demonstration of the multiscale approach, which combined first-principles calculations, a mixed-space cluster expansion approach, and the diffuse-interface phase-field model. Many other kinds of computer simulation methods are developed vigorously, such as the first-principles (FP) calculation, molecular dynamics (MD) simulation, Monte Carlo (MC) method, and phase-field method. Generally, the FP calculation, MD simulation, and MC method are thought to be suitable for the analysis of nanostructure and properties, since these three models are all the typical simulation methods for material behaviors at atom and molecular scales; however, FP calculation only uses three basic physical constants, the Planck constant, electron mass, and electronic volume, and arrangement of atomic extranuclear electrons for the sake of precision, to solve the self-consistent Schrodinger equation,[11] which makes the calculation labor intensive and only handles a limited number of atoms (about 1000 atoms) according to the computing capacity of computers at present. MD simulation also requires solution of the Newton's equation for all particles, in order to obtain the dynamic characteristics of the system;[12] its typical simulation time is in the range of

picoseconds. The MC method is a random method for numerical integration; the classical MC method is not related to trajectories, only calculates the equilibrium thermodynamic quantities, and cannot predict the dynamics of nanostructure materials.[13] Frost *et al.* improved the Potts model to simulate the grain growth process, but it still consumes a large amount of computing time for the selection of random grid points. The simulated time is usually represented by the MC steps.[14] However, the variety of multiscale modeling applications combine different types of models with different principles, which may confuse the physical nature of an application and may result in a numerical fitting phenomenon without an understanding mechanism. It may be ideal to find a multiscale grain growth model based on one method, and the phase-field model is probably the only possibility in analytical physics nature.

Phase-field methods are based on microscopic and continuum diffusion equations. However, the conventional microscopic phase-field model uses the probability of the solute atom occupying the given lattice sites at a given time as the variable field and does not have an expression of the local free energy density. The kinetic parameters need to be related to the phenomenological diffusion coefficient in the continuum model in order to compare the simulated results with experimental measurements, and the time and space scales of the microscopic phase-field model after Fourier transformation are 10^{-9} to 10^{-6} m and 10^{-6} to 10^{-3} seconds,[15] which cost much calculation time. However, for the continuum phase-field model, due to the use of the gradient of the conservation and nonconserved field variables (such as concentration, structure, orientation, long-range order, *etc.*) to describe the diffusion interface between each phase, there is no sharp interface, which truly achieves the description of the migration of the diffusion boundaries. So the continuum phase-field model is chosen in our article in an attempt to cover multiple scales in grain growth.

After many researchers' hard work, phase-field simulations became increasingly more sophisticated both in numerical calculation and practical application; for example, Karma and Rappel[16,17] developed the thin-interface limit for modeling the solidification of a pure material by phase-field method for efficient computations. Reference 18 shows that they formulated the first phase-field model of evolution of a multidislocation system in elastically anisotropic crystal under applied stress. Reference 19 includes the attempted development of a phase-field model into a quantitative tool to simulate the microstructural transformation under a certain heat treatment process. Böttger *et al.*[20,21] applied the multiphase-field method coupled to thermodynamic databases and experiments as an engineering approach to describe equiaxed solidification and solid-state transformation for technical AZ31 Mg alloy. Our recent previous work already achieved a phase-field model to simulate the grain growth process during recrystallization of AZ31 alloy in real time and space, and the simulated results agree well with the experiments[22–26] by introducing a new concept of the grain boundary range. It is believed that the model is the first time a grain growth simulation of realistic spatiotemporal evolution of microstructure in industrial scale was accomplished. However, as far as the authors know, no phase-field model of the nanoscale grain growth process in a real alloy has been reported.

In this article, a modification of our previous phase-field model is reported to simulate the multiscale grain growth in polycrystalline AZ31 Mg alloy in the realistic spatiotemporal process. The driving force is discussed again, and the parameters are varied systematically to find the possibilities to form the expected structure in order to model the grain growth from nanoscales to micron scale. Comparisons of the simulated results with the experiments at different temperatures are made to explain the mechanisms of the grain growth especially in nanostructure to establish references for the development of the nanocrystalline materials.

II. PHASE-FIELD MODEL IN MULTIPLE SCALES

A. *Model Fundamentals*

Magnesium alloys have gained great attention in recent years for their high specific strength, high specific stiffness, low specific weight, and low pollution, but they have poor plasticity and strength. As we know, grain refining is a general way to improve both mechanical strength and ductility of metallic materials. A bulk nanocrystalline Al-5 pct Mg alloy revealed that it has 4 times the strength of a conventional Al-5083 alloy along with good ductility (8.5 pct elongation).[2] In present simulations, AZ31 Mg alloy was chosen as the study material with the concentration of (in mass) w (Al) = 3 pct, w (Zn) = 1 pct with the remainder magnesium.

Phase-field methods are based on thermodynamics and kinetics. The temporal evolution of microstructure can be determined by solving the time-dependent Allen–Cahn equation and Cahn–Hilliard diffusion equations as follows:[27,28]

$$\frac{\partial \eta_j(\mathbf{r},t)}{\partial t} = -L\frac{\delta F}{\delta \eta_j(\mathbf{r},t)}, \quad (j=1,2,\ldots,n) \qquad [1]$$

$$\frac{\partial c(\mathbf{r},t)}{\partial t} = M\nabla^2\frac{\delta F}{\delta c(\mathbf{r},t)}$$

where L and M are the structural relaxation and chemical mobility parameters, respectively, η_j ($\mathbf{r}$, t) is the long-rang orientation parameters, c ($\mathbf{r}$, t) is a concentration field variable, F is the free energy of the system, and its expression in isotropic single-phase system is seen as follows:[29]

$$F = \int \left[f_0(c,\eta_1(\mathbf{r},t),\eta_2(\mathbf{r},t),\ldots,\eta_p(\mathbf{r},t)) + \frac{K_2}{2}\sum_{i=1}^{p}(\nabla\eta_j(\mathbf{r},t))^2 \right] d^3\mathbf{r} \qquad [2]$$

where K_2 is the gradient energy coefficient and f_0 is the local free energy density function.

B. *Grain Boundary Range*

Reference 29 claims that the sharp-interface models were inappropriate for describing grains with sizes close to the boundary width, and the diffuse-interface field models have already been proposed to describe a polycrystalline microstructure by many orientation field variables.[29–32] In these models, grain boundaries are assumed to be diffuse with finite thickness, and their width is actually the range of field variables changed across the flat grain boundary. However, limited by the actual physical thickness of grain boundary thought to be a few lattice parameters (for example, 20Å), the parameters in the models were assumed as numerical values. Later, as shown in References 19, 33, and 34, an artificially diffuse interface at the length scale of practical interest was produced, for example, an increase the interface width from about 9 to 36 nm,[34] without altering the kinetics and microstructure along the evolutionary path. However, the interface width is still too small for large grains on the order of micrometers and long time for hours in engineering scaling scope. The interface thickness condition was also discussed in the phase-field model of solidification,[16,17,35,36] and Karma *etc*. presented the thin-interface limit analyses, which allowed the width of the diffuse interface to be larger than about an order of magnitude of the capillary length.[16,17]

Therefore, we proposed a new concept, called "grain boundary range,"[22–24] to define the distance of the gradient variation of the long-range orientation parameters across an interface. The "interfacial width" in phase-field simulation should be optimally chosen to satisfy both the precision and required computational efficiency, so that our grain boundary range is the same as the interfacial width. However, the interfacial width has a different meaning in material science: it is the geometrical width of an interface in a scope of 3 to 5 atoms thickness. If we take the phase-field "interfacial width" as 3 to 5 atoms, the phase-field simulation does not have computational efficiency. We suggested that the phase-field interfacial width can be as large as up to micrometers, and we suggested the new term "range" instead of width for clearance. Moreover, our study[22–24] finds that the range has a physical concept of the region around an interface, which the interface affects *via* interface energy and interfacial element segregation. The boundary energy of a low-angle grain boundary, for example, consists chiefly of elastic strain energy, and it is formed by a series of dislocations whose effective elastic field is up to a micrometer in size. The position of the interface defined in our model is the geometric center of symmetry of the grain boundary range. The variation of η across a flat boundary was calculated by the present multiscale model in micron grains, and it is shown in Figure 1(a). The grain boundary range r in the microstructure can be measured from Figure 1(a), and it is indicated by the scale bar in the figure and is about 1.2-μm wide.

The value of grain boundary range 1.2 μm is too large for grains in nanoscales whose grain size is less than 1 μm, and the grain boundary range will have no physical meaning if it covers more than two grains. The volume fraction of grain boundaries increases dramatically when the grain size decreases,[37] and Reference 38 shows that the nanocrystalline materials might consist of over 50 pct of geometric boundary regions (interface component) depending on the average grain size. Therefore, we suggest that the nanocrystalline materials will have a grain boundary range that covers up to nearly two whole adjacent grains, as seen in Figure 1(b). However, we only take one grain area when we calculate the boundary energy so that any boundary energy will not be counted twice for the neighboring boundaries, although the boundary ranges of a grain share some regions with their neighbors. The simulated results

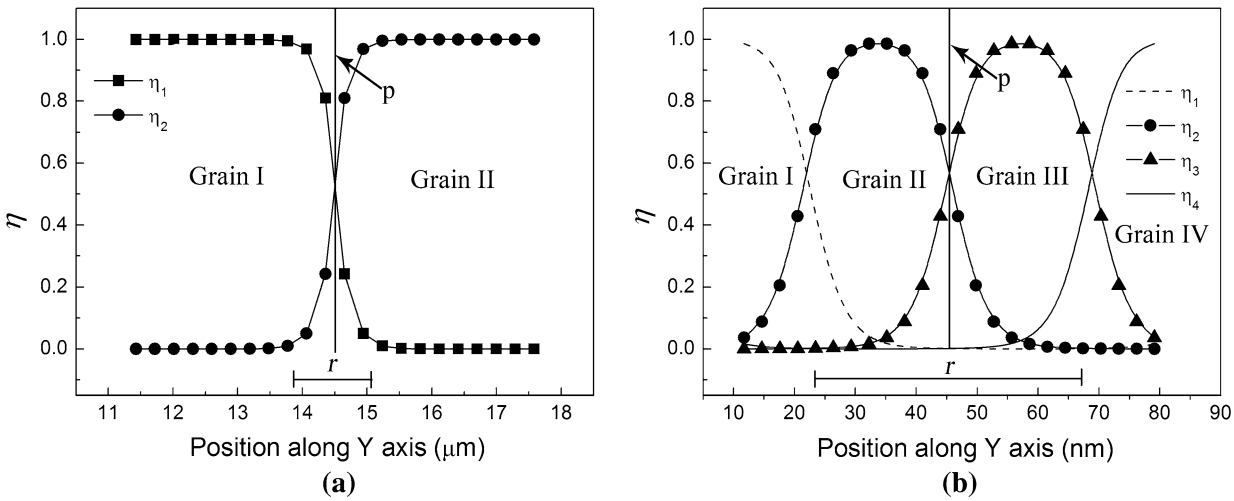

Fig. 1—Characteristics of grain boundary in orientation parameters by simulations: (*a*) for micron scale model and (*b*) for nanoscale model. *p*—grain boundary position; *r*—the grain boundary range.

Table I. Values of Grain Boundary Range r at Each Scale

Average grain size (nm)	Grain Boundary Range, r (nm)
24 to 85	47
86 to 219	164
220 to 1000	434
Larger than 1000	1172

Table II. Values of B_1 and B_2

Average Grain Size (nm)	B_1 (kJ/mol)	B_2 (J/mol)
24 to 85	80.33	2321.51
86 to 219	22.95	663.29
220 to 1000	8.68	250.77
Larger than 1000	3.54	92.86

based on such a range model of variation of η across a flat boundary are shown in Figure 1(b) in the nanostructure by our present multiscale phase-field model.

It is also seen from Figure 1(a) that the values of η_j (j represents a certain orientation of the grains) vary in one grain from 1 to 0 into another grain gradually across the grain boundary range. However, the grain boundary range covers its adjacent two grains in nanoscale in Figure 1(b), which means that the attribution of the orientation of a grain may be influenced not only by itself but also by its nearest neighbors. It is the size and the physical character of the boundary range that makes the key difference in our present model for different scale applications.

The boundary range cannot be varied automatically when the grain size increases with increasing annealing time by the computing code of our present model. In order to improve the computational efficiency, the multiscale grain growth process for AZ31 Mg alloy was divided into four stages from nanoscales to micron scale. Simulations were carried out to find the proper size of the range for each stage, and the results of the grain boundary range r are listed as a function of grain size in Table I. The computing code would be broken several times automatically to check average grain size to adjust the range values according to Table I if necessary during the grain growth simulations.

C. *Local Free Energy Density Function*

The local free energy density function f_0 represents the figuration of a phase-field model, and the basic requirement for it is that f_0 has p degenerate minima located at $(\eta_1, \eta_2, \ldots \eta_p) = (1, 0, \ldots, 0), (0, 1, \ldots, 0), \ldots, (0, 0, \ldots, 1)$.[29] We adapt an expression to describe the local free energy density function as follows:[22]

$$f_0 = A + A_1(c(\mathbf{r},t) - c_l)^2 + \frac{A_2}{4}(c(\mathbf{r},t) - c_l)^4 - \frac{B_1}{2}(c(\mathbf{r},t) - c_l)^2 \sum_{i=1}^{p} \eta_i^2(\mathbf{r},t) + \frac{B_2}{4}\left(\sum_{i=1}^{p} \eta_i^2\right)^2 + \frac{K_1}{2}\sum_{i=1}^{p}\sum_{j\neq i}^{p} \eta_i^2(\mathbf{r},t)\eta_j^2(\mathbf{r},t) \quad [3]$$

where c_l is the concentration at the lowest point of the free energy curve as a function of concentration at a certain temperature, K_1 is the coefficient of coupling item between η_i and η_j, and p is the possible number of the grain orientations in the system and is taken as 32, as suggested in Reference 29.

In order to keep f_0 minimal at $\eta_i = 1$ and $\eta_j = 0$, the derivation of Eq. [3] has to be zero, and the relationship of B_1 and B_2 is $B_1 (c - c_l)^2 = B_2$.

Assuming that $\eta_j^2 = 1$ with $\sum_{i\neq j}^{p} \eta_i^2 = 0$represents the orientations in grains and $\sum_{i=1}^{p} \eta_i^2 = 0$ represents the initial state that is amorphous solid, we suppose that the initial state can be simplified as the large-angle random grain boundary body. The $f_0\left(\sum_{i=1}^{p} \eta_i^2 = 0\right) - f_o\left(\eta_j^2 = 1, \sum_{i\neq j}^{p} \eta_i^2 = 0\right)$ represents the energy difference contained in a unit mole between the amorphous solid and crystallization. The thickness of a unit random boundary can be taken as the boundary range. Since the grain boundary energy is the accumulation of energy in the boundary range in the phase-field model, and only a small part of the region in the boundary range contains the large value of grain boundary energy, while in the rest of the region, the energy is small, we actually calculate the thickness with one-fourth boundary range. Therefore, the constants can be determined as follows:

$$H = f_0\left(\sum_{i=1}^{p} \eta_i^2 = 0\right) - f_o\left(\eta_j^2 = 1, \sum_{i\neq j}^{p} \eta_i^2 = 0\right) = \frac{\sigma M}{(1/4) r \rho} = \frac{B_1}{2}(c - c_l)^2 - \frac{B_2}{4} \quad [4]$$

where σ is the random grain boundary energy, M is the molar mass of AZ31 Mg alloy, and ρ is the density. The random grain boundary energy of 0.5 J/m^2 is used only for defining the initial state. The value of boundary energy here has no relationship with grain size and with real grain boundary energy in microstructure simulated later. Therefore, B_1 and B_2 are obtained by relating to the grain boundary energy and Eq. [4]. The calculated results are listed in Table II as the range is varied according to the average grain size.

On the other hand, in the Mg-Al-Zn alloy system, the free energy-concentration curves can be obtained by the software THERMOCALC (Thermo-Calc Software AB, Stockholm Technology Park, Stockholm, Sweden) at different temperatures according to the corresponding experimental database;[22,23] the curves are given in Figure 2(a).

According to Figure 2(a), c_l is obtained to equal 0.2 at 573 K and 623 K (300 °C and 350 °C), respectively. The best values of A, A_1, and A_2 are obtained by fitting the curves in Figure 2(a) with Eq. [3] when $\eta_j^2 = 1$ and $\sum_{i\neq j}^{p} \eta_i^2 = 0$ at each scale, and the optical results are shown in Table III. The corresponding fitting curves are given in Figure 2(b) by fitting Eq. [3] using the values of the parameters listed in Table III, and they show a good match with the experimental data in Figure 2(a).

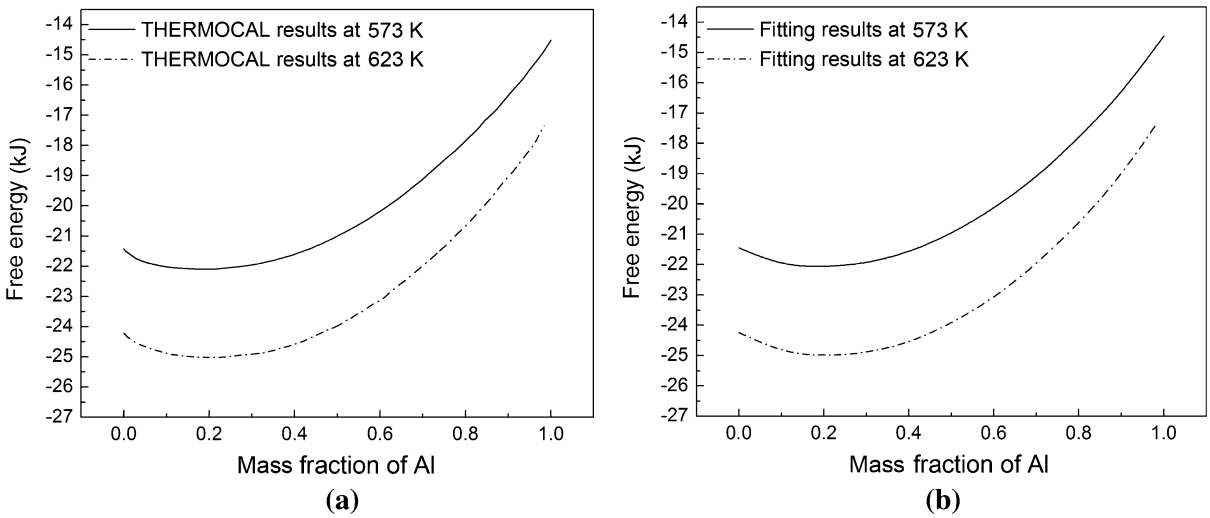

Fig. 2—Free energy-component curves of AZ31 Mg alloy obtained by the software THERMOCAL and fitting results: (*a*) for THERMOCAL results and (*b*) for fitting results.

Table III. Best Fitting Values of A, A_1, and A_2 at Different Temperatures in Eq. [3]

Average Grain Size (nm)	A (kJ/mol)		A_1 (kJ/mol)		A_2 (kJ/mol)	
	573 K (300 °C)	623 K (350 °C)	573 K (300 °C)	623 K (350 °C)	573 K (300 °C)	623 K (350 °C)
24 to 85	–22.67	–25.57	99.64	99.14	13.00	18.30
86 to 219	–22.25	–25.15	42.26	41.76	13.00	18.30
220 to 1000	–22.15	–25.05	27.99	27.49	13.00	18.30
Larger than 1000	–22.11	–25.01	22.52	22.02	13.00	18.30

D. *Grain Boundary Energy*

According to the theory of flat interface energy in the isotropic system proposed by Cahn and Hilliard, the flat grain boundary energy σ between two grains whose orientations are, respectively, i and j, can be expressed as follows:[28]

$$\sigma = \int_{-\infty}^{+\infty} \left[f_0 - f_{\text{Min}} + \frac{K_P}{2}\left(\frac{d\eta_p}{dx}\right)^2 + \frac{K_q}{2}\left(\frac{d\eta_q}{dx}\right)^2 \right] dx \quad [5]$$

where f_0 is the value of free energy density near the boundaries, f_{min} is the constant in grains far away from the boundaries, K_p and K_q are the gradient parameters of p and q orientations, and $K_p = -K_q = K_2$ is expressed in our model here in the isotropic system. Our model does not consider the anisotropic interface energy for the simplification of the model. The anisotropic grain boundary energy may lead to the abnormal grain growth and have a great impact for the metastable phase, but have only a small influence at high-temperature aging.

The coupling item parameter K_1 and the gradient parameter K_2 in the local free energy density function are dependent on the grain boundary energy and the grain boundary range. A bi-crystal figuration is used to study the relationship between K_1, K_2, and the features of the boundary range and grain boundary energy for polycrystalline AZ31 Mg alloy. The simulated results are shown in Figure 3. The first three columns of data are the relationship of the grain boundary energy and the grain boundary range with variations of K_1 and K_2 when the grain size is less than 85 nm. The second three columns of data are for the grain size between 86 and 219 nm, and the rest of the columns of data are for the grain size between 220 and 1000 nm.

In our previous work,[22–24] we obtained the phase-field model for the process of grain growth for microcrystalline structure AZ31 Mg alloy, and the simulated results showed that the boundary range was mainly decided by K_2. However, in our present model, the boundary range is determined both by K_1 and K_2, and it may be for that reason that the grid size set in our model in nanoscales is 2.93 nm, which is much smaller than that in the micron scale model with size of 293 nm. Meanwhile, the micron scale model has a value of grain boundary energy of 0.55 J/m^2, and the grain boundary range is a constant of about 1.17 μm. In our present new model, when $K_1 = 141.24$ J/mol and $K_2 = 3.54 \times 10^{-12}$ m^{2}J/mol, it can satisfy the requirements.

K_1 and K_2 have to be varied according to Figure 3 of the simulated results to meet the different values of the

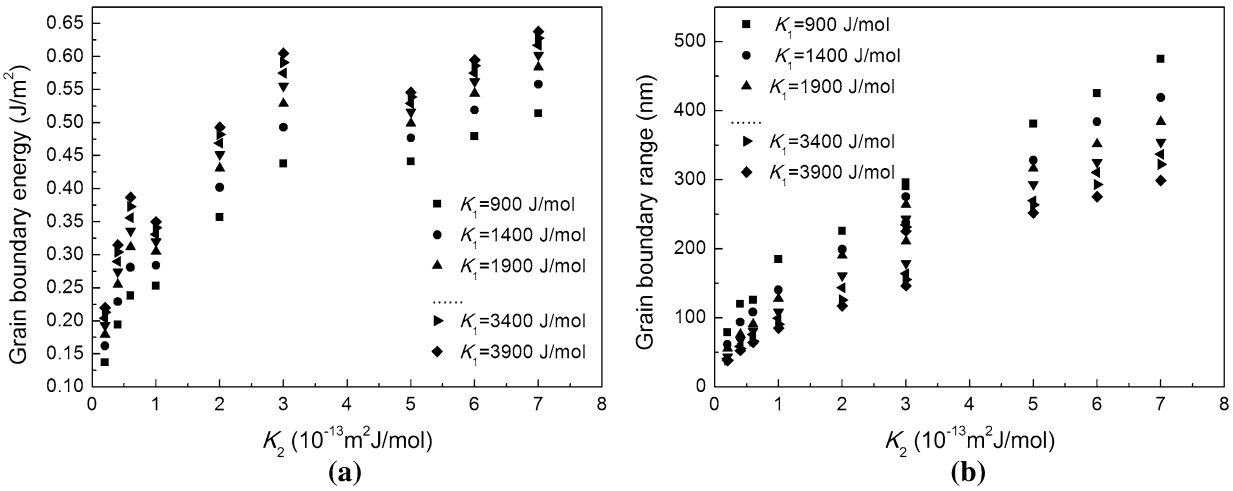

Fig. 3—Relationship between K_1, K_2, and the relevant grain boundary features in the nanoscales: (*a*) for the grain boundary energy and (*b*) for the grain boundary range.

Table IV. Values of K_1, K_2, and σ in Multiscale Model, Compared with Experimental Data

Average Grain Size (nm)	K_1 (J/mol)	$K_2 \times 10^{-13}$ (Jm^2/mol)	σ* (J/m^2)	D_m^{**} (nm)	σ_m^{**} (J/m^2)
24 to 85	2090.16	0.21	0.19	18.75 to 26.51	0.18 to 0.19[39]
86 to 219	1103.14	1.29	0.30	86 to 112	0.22 to 0.34[40]
220 to 1000	1045.08	6.23	0.50	225 to 260	0.48 to 0.52[40]
1000~	141.24	35.37	0.55	1000~	0.55[22,23]

*σ is the grain boundary energy by our phase-field calculations.
**D_m and σ_m are the measured average grain size and grain boundary energy, respectively, in the references.

boundary range and the boundary energy in different scales. The proper values of K_1 and K_2 in our multiscale model are listed in Table IV.

It is seen in Table IV that values of the grain boundary energy by simulations decrease significantly with decreasing grain size down to nanoscales due to the physical nature of the present phase-field model with a small value of the boundary range when the grain size is small. The simulated results are proved by the experiments shown in Table IV, which not only indicates the great success of our present model but also supplies an explanation of the phenomena implied by very limited experimental measurements. It may not be easy to believe that the boundary energy is small when the grain size is small unless one considers that nanoscale grains are too small to accommodate Frank–Read dislocation sources, which would lead to runoff of a part of the distortion energy, which would contribute much less to the boundary energy. In addition, Lu in Reference 40 suggested another possible reason for the phenomenon; *i.e.*, the grain boundary energy of the nanograined copper by means of dynamic plastic deformation decreases with decreasing grain size.

E. *Other Model Parameters*

L is the coefficient related to grain boundary mobility, and it was explained in the micron scale model in detail that the value was 1.15×10^{-2} mol/J s at 623 K (350 °C) and 7.25×10^{-3} mol/J s at 573 K (300 °C)[22,23] by matching the simulated results with the experiments. We used the same method to obtain the values of L in the nanostructure too. The average grain sizes measured[41] during grain growth at 623 K (350 °C) were used as the target curves, and the simulated results by our present model were carried out with different L to match the curves. It was found that when $L = 2.07 \times 10^{-6}$ mol/J s at 623 K (350 °C), the simulated results of grain size as a function of time can match the curves shown in Figure 6(a). According to the Arrhenius formula that $L = L_0 \exp(-Q/\mathrm{R}T)$, where $Q = 27.6$ kJ/mol as the Al segregation activation energy given by References 22 and 23, it is calculated that $L_0 = 4.26 \times 10^{-4}$ mol/J s by the preceding value of L at 623 K (350 °C), and then the value L at 573 K (300 °C) is calculated as 1.30×10^{-6} mol/J s.

In the mean field approximation, M is the diffusion mobility, and according to Reference 31, it has a relationship with the diffusion coefficient D in a dilute solution that $M = (1 - c_0)\, c_0 D/\mathrm{R}T$, where c_0 represents the mean concentration of the alloy, R is the gas constant, and T is the absolute temperature.

The diffusion coefficient of aluminum in the magnesium matrix is $D = 1.2 \times 10^{-3} \exp(-143{,}000/\mathrm{R}T)$ m^2/s, so $M = (1 - c_{\mathrm{Al}})\, c_{\mathrm{Al}} D/\mathrm{R}T = 6.91 \times 10^{-21}$ m^{2}mol/J s at 623 K (350 °C) and $M = 6.75 \times 10^{-22}$ m^{2}mol/J s at 573 K (300 °C), respectively, for conventional grain growth of micron scale. However, M has a relationship with L so that $x = M/Ll^2$, where l represents the grid spacing,[31] so the values of M in nanoscales have to be

adjusted. The mobility constant x controls whether the grain growth is diffusion or interface controlled, and in order to ensure interface-controlled growth in the case of grain growth, the value of x has to be relatively large and we take a proper value of 7×10^{-2} proved by our previous work.[22,23] Therefore, the value of M is 1.24×10^{-24} m^2mol/J s at 623 K (350 °C) and 7.81×10^{-25} m^2mol/J s at 573 K (300 °C) in nanoscales in our present model.

The parameter M is not dependent on L in our simulation, and our model only tries to adopt all real experimental parameters to simulate real grain growth. We always used actual diffusion parameters found in the references in our work, although there are comments in our article citing that much of the research supposed a dependent relationship between M and L.

F. *Initial Condition Setup*

The nucleation process of crystallization is simplified by a phenomenological method, and the well-defined grain microstructure is formed after a short time. The initial state is given as the $4dx \times 4dx$ unit distributing evenly in the simulated area, and the radius of the nucleus is a random value between 0 to 2 grids. Our simulations are conducted in the 512 × 512 two-dimensional uniform grids.[29] The overall size of the simulation cell is 1.5 μm × 1.5 μm at nanocrystalline structure with each grid size being 2.93 nm, whereas for the micron scale model, the unit grid size is 0.293 μm and the entire simulation area is 150 μm × 150 μm. The local initial composition is considered as 0.03. The value of the time-step has to be relatively small in order to obtain the convergence results; however, an extremely small value of time-step will require more steps for solving the kinetic equations. The values of 0.6 seconds in the nanoscales model and 0.3 seconds in the micron scale model for time-steps are chosen to balance the two factors. The boundary condition of the differential equations is defined as the periodic boundary, in order to minimize the boundary effect on the grain growth kinetics.

III. SIMULATED RESULTS AND DISCUSSION

A. *Multiple Scale Grain Growth in Different Temperatures*

The morphology and evolution of the polycrystalline structure in the AZ31 alloy were simulated by our phase-field model during annealing time, and the results are shown in Figure 4. The values of all simulated parameters were obtained from physical analysis or experiments in our model presented in Section II, so that the results in Figure 4 are all in real time and real scale. Therefore, the grain size can be compared with the actually measured results by experiments directly.

It is seen in Figure 4 that the grain structures based on the orientation field and the concentration field at the same time are identical both in nanostructure and micron structure, which is a proof of the validity of our phase-field model. However, the concentration field shows a variation pattern in large grains in Figure 4(h), for example, and this suggests that a grain only large enough to 10 μm in diameter can have the character that the boundary energy may vary significantly with different crystal orientation neighbors. There are some great elongated grains in nanoscale, as given in Figures 4(a) and (c) shown in circles, and they are proof of a grain coalescence mechanism of coupling grain rotation during grain boundary migration. On the other hand, the grains in micron scale always show the round polygonal shape, which exposes some differences of grain growth mechanisms in nanoscale compared with micron scale. Several large grains can be seen in the fine grains in Figures 4(a) and (c) in nanostructure, and these grains imply a tendency of easy abnormal grain growth in nanostructure.

The distribution of grain size both in nanostructure and micron structure was examined, and the statistical results are shown in Figure 5. It is found by comparing Figures 5(a) and (b) that the distribution of grain size in nanostructure is symmetrically close to the average size (66 nm) in the maximum content size (59 nm) with a few very large grains, whereas the distribution of grain size in the micron structure is a random narrow shape far away from the average size (21 μm) in the maximum content size (17 μm). The differences in the distribution of grain size cause the differences in grain growth kinetics between nanostructure and microstructure presented in Section III–B.

In order to check the reliability of the simulations, we compared the simulated results of grain growth with the experimental results at different temperatures, as shown in Figure 6. It is seen that the simulated results are matched well with the experimental data at 623 K (350 °C). However, the simulated results are not matched very well with the experiments at 573 K (300 °C) in Figure 6(a) in nanostructure, which may imply a different mechanism in activity energy at lower temperature.

B. *Grain Growth Kinetics*

Conventional grain coarsening in single-phase polycrystalline materials is a migration process of grain boundaries, driven by the mean curvatures. Generally, it is thought to obey the parabolic kinetic equation, such as Hillert's theory,[42] which predicted a time exponent n of the highly pure materials in grain growth as $n = 2$. The equation is as follows:

$$D^n - D_0^n = kt \qquad [6]$$

where t is the evolution time, D is the average grain size in diameter, D_0 is the initial average grain size, and k is a temperature-dependent rate constant. However, the time exponent n is often deviated from the value 2 for practical reasons, Reference 41 showed $n = 5$ for the grain growth in nanocrystalline AZ31 Mg alloy.

Our model has a particular advantage in examining grain growth kinetics over a large size scale, because it can simulate the growth from nucleation to an enormous artificial annealing time at a low temperature.

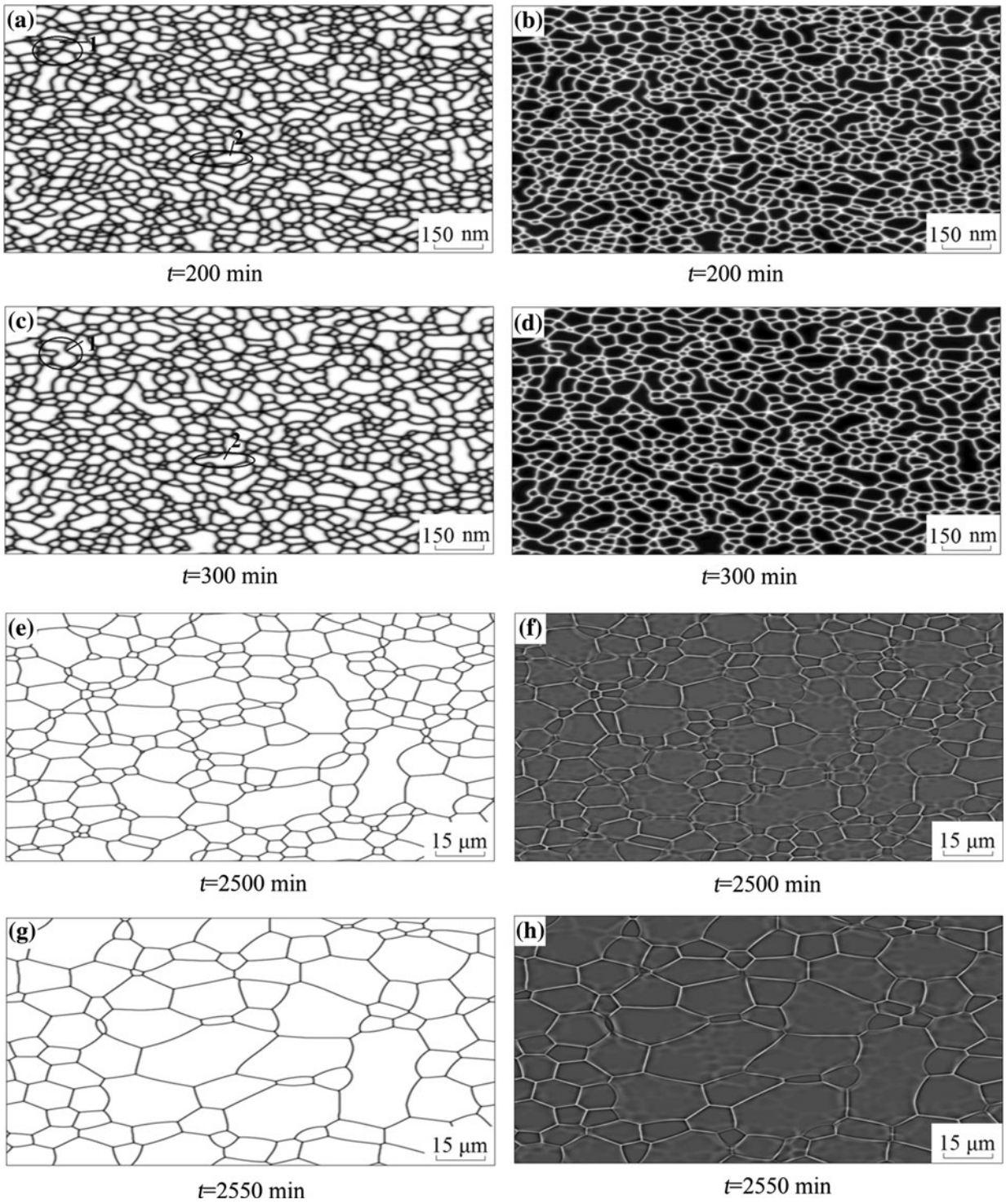

Fig. 4—Simulated results of grain growth both in nanostructure and microstructure when t = 200, 300, 2500, and 2550 min, respectively, at 623 K: (*a*) through (*d*) for nanostructure; (*e*) through (*h*) for microstructure; (a), (c), (e), and (g) in orientation field; and (b), (d), (f), and (h) in concentration field.

Such simulated results of AZ31 Mg alloy at 623 K (350 °C) are shown in Figure 7 with some experimental results[41,43] for comparison, as follows.

It is seen in Figure 7 that the increase of average grain size is more obvious in microstructure than that in nanostructure. The grain growth essentially obeyed the power law at n = 5 in Eq. [6] in the early process of grain growth. The grain growth rate is very slow in the initial stage in nanostructure, and this is a surprising and interesting result. Since n is a large value of 5 in the stage, it is believed that the phenomenon has a sensitive temperature dependence; *i.e.*, the nanoscale grain growth

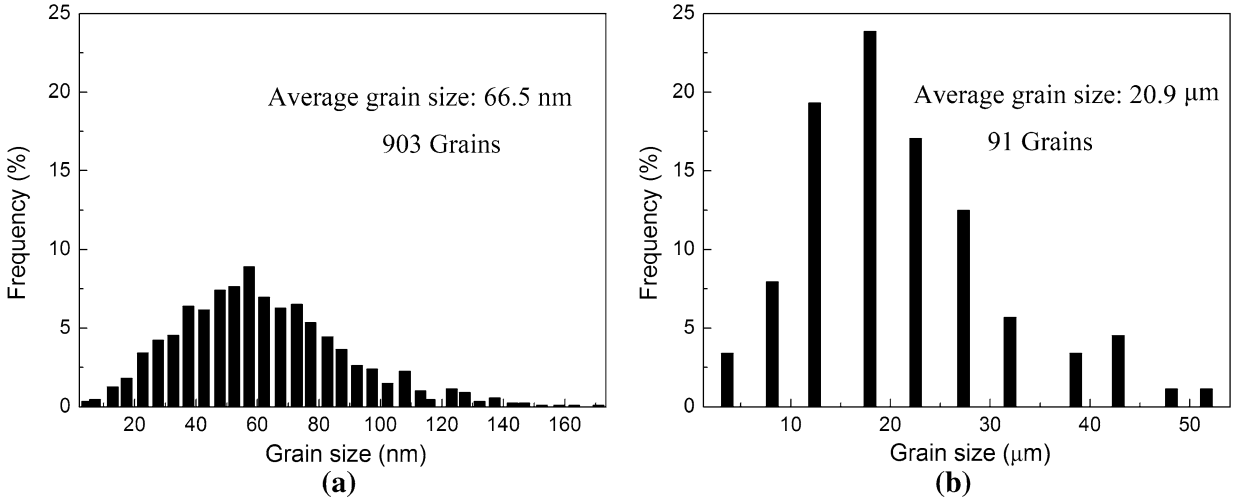

Fig. 5—Distribution of grain size for nanostructure and microstructure by simulations at 623 K and the annealing time t = 200 and 2550 min, respectively: (*a*) for nanostructure and (*b*) for micron structure.

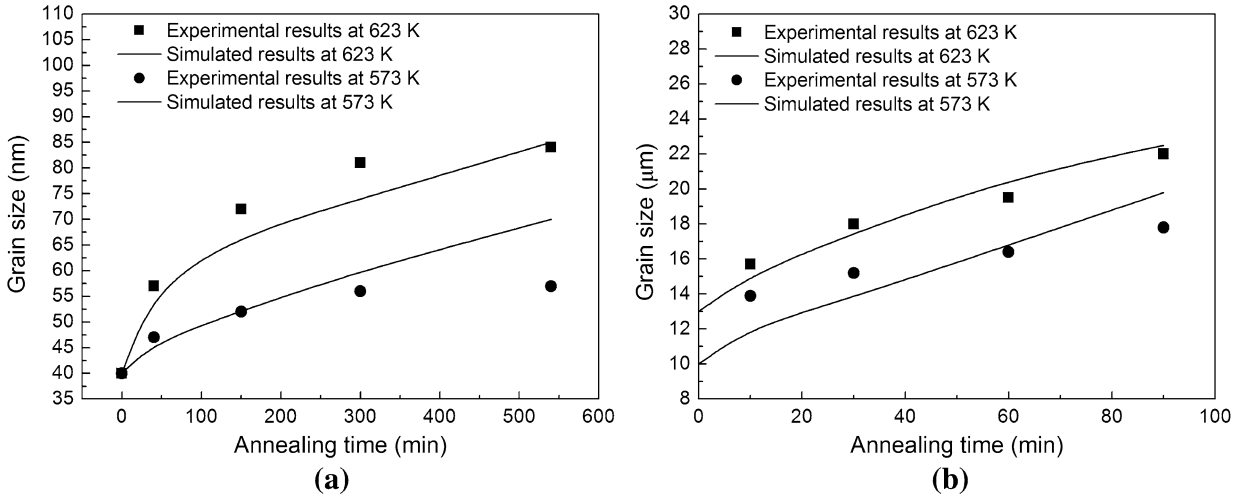

Fig. 6—Simulated average grain size evolution in nanoscale and micron scale as a function of annealing time compared with the experiments in Refs. [41] and [43] for AZ31 Mg alloy.

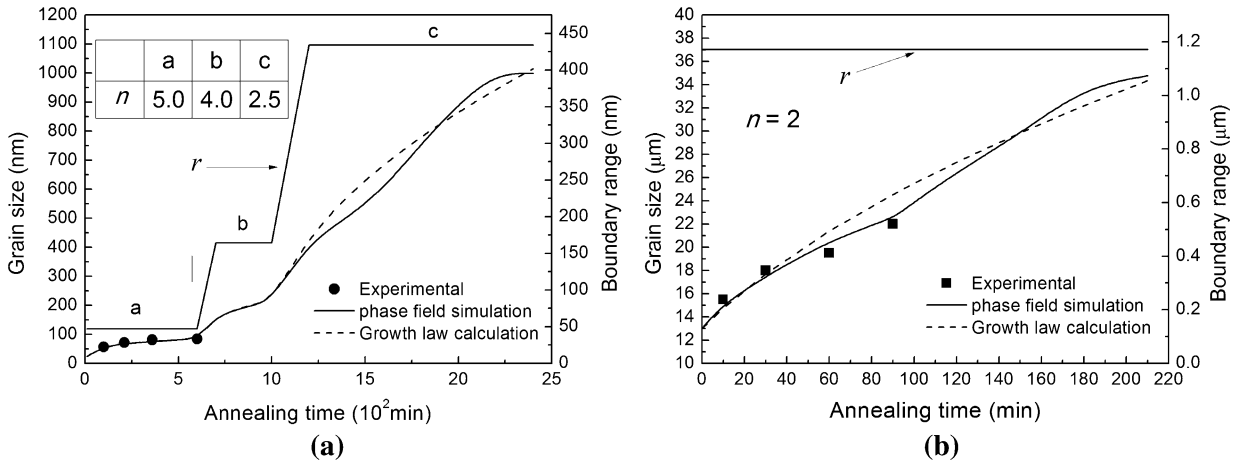

Fig. 7—Simulated average grain size evolution of nanoscales and micron scale as a function of the annealing time compared with the experimental results in Refs. [41] and [43]: (*a*) for the evolution of nanoscales and (*b*) for the evolution of the micron scale. r is the boundary range.

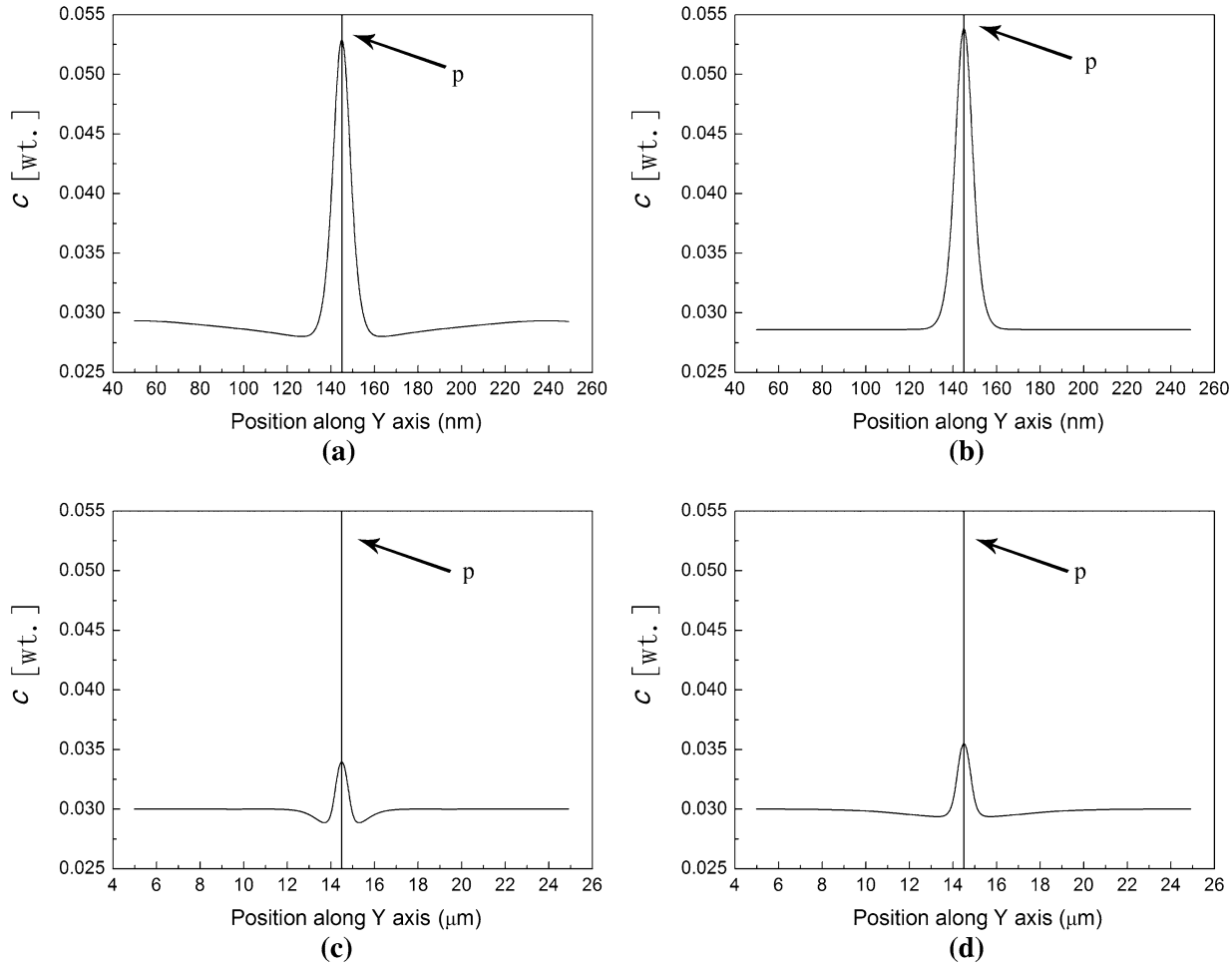

Fig. 8—Simulated results for segregation of Al element at grain boundaries in nanostructure and microstructure for AZ31 Mg alloy at different temperatures: (*a*) nanostructure at 573 K, (*b*) nanostructure at 623 K, (*c*) microstructure at 573 K, and (*d*) microstructure at 623 K. *p*—grain boundary position.

kinetics is affected more significantly by the annealing temperatures than by micron scale. It is also seen that n decreases with the increase of the average grain size during grain growth, and it becomes the normal to 2 when the growth enters the conventional grain coarsening stage of micron scale. This indicates that the mechanisms of the grain growth are not the same at different grain size scales. These findings are also proven by the limited experimental results[44] that the grain growth curves were fitted much better to the kinetic equation in two separate parts with different n values than that in a single n value part in nanocrystalline Fe produced by high-energy ball milling.

Table IV has shown that the values of K_1 and K_2 are different at different grain size scale stages and K_2 is smaller in nanoscales than that in micron scales. The grain boundary energy is decided by K_1 and K_2, and the calculated grain boundary energy in nanoscales is lower down to about a half that in the micron scale. Meanwhile, the coefficient L related to the grain boundary mobility in nanostructure is also smaller than that in micron structure. The two kinetic and thermodynamic aspects may lead to the slower grain growth rate for nanoscale polycrystalline AZ31 Mg alloy.

C. *Alloying Element Segregation at Grain Boundaries*

In order to explain the physical reasons for the slower growth rate of grains in nanostructure than that in the micron structure, the behaviors for alloying element segregation at the grain boundaries are further studied by simulations. The distribution of the concentration of element Al in AZ31 Mg alloy was studied across a flat grain boundary at different temperatures with grain size about 85 nm and 35 μm. The results are shown in Figure 8.

It is seen in Figure 8 that the concentration of Al is much higher in the grain boundaries than that in the grains, and the segregation range of grain boundaries for grains in micron scale is larger than that in nanoscale. The simulations expose that the solute atoms would prefer to segregate at the boundaries much more severely in nanostructure than in microstructure, though the dependence of segregation on the temperatures is the same in both structures. The phenomenon that the segregation level would decrease with the increase of grain size was reported by an experimental study of phosphorus segregation in nanocrystalline Ni-3.6 pct P alloy investigated with the tomographic atom probe.[45] The simulation

results show that the AZ31 magnesium alloy polycrystalline has the size effects of boundary segregation. The nanostructure materials show higher segregation, because there are a large number of interfaces to provide extra free energy to promote diffusion and a high density of short circuit diffusion paths. The adsorption capacity is quite high (high solute solubility) and the solute atoms may trap easily and, therefore, diffuse less through the bulk in nanostructure materials.[46] Nevertheless, the phase-field model has the advantage of showing the nature of microstructural evolution, including diffusion, which gives a much higher value to the results of the size effect obtained by our simulation. Our model simulates diffusion phenomena based chiefly on thermodynamics. The uphill diffusion of the segregation in our simulation is not only affected by the kinetic diffusion coefficient, but also mainly affected by the contribution of the diffusion driving force. In fact, the diffusion coefficient in our model is the same both for micron meter and nanometer microstructures but different local free energy functions. Therefore, our simulation indicates that the size effect is due to thermodynamic driving force rather than dynamic mobility. Essentially, the expression of the local free energy density function leads to the occurrence of severe uphill diffusion, because the nanostructure has higher local free energy density contributed by multiple gradient terms of long-range orientation field parameters. The solute atoms segregated to the boundaries will lead to the retarding force on the boundary migration,[47] which finally results in the slower grain growth in nanostructure.

Apart from the low grain boundary energy and different growth dynamics, the mechanisms of nanograin growth include that diffusion plays an important role. This can be explained by the finding that the volume fraction of grain boundaries increases dramatically when the grain size decreases, which will result in high diffusion path and short diffusion distance to realize element segregation at boundaries by low-temperature diffusion during the age annealing in our simulation, and the segregation will significantly change the boundary mobility.

IV. CONCLUSIONS

1. A multiscale phase-field model is established to simulate the realistic spatiotemporal grain growth for AZ31 Mg alloy by varying the local free energy density function and the gradient parameters according to different growth driving forces. The simulated results agree well with the experiments both in nanoscale and micron scale.
2. Simulated results show that the grain boundary range for grains in nanoscales covers no more than two adjacent grains from about 40 to 400 nm, while the range should be a constant large value of about 1.2 μm for grains in micron scale.
3. The modeling shows that the grain boundary energy in nanocrystalline alloy is lower down to about a half that in microcrystalline alloy and the time exponent n in the kinetic equation is varied from 5 to 2 from the nanostructure to the microstructure. These findings can be proved by the limited experimental results found in the literature.[41,43]
4. It is found that the grain growth rate in nanoscales is much slower in an order of magnitude than that in the micron scale, and it is inconsistent with the experimental results. The lower grain boundary mobility and lower grain boundary energy in the nanostructure are suggested as the reasons.
5. Simulations expose that solute atoms segregate at the grain boundaries much more severely in nanostructure than in conventional micron structure, though the dependence of segregation on temperatures is the same in both structures. This may be the reason why nanostructure shows a lower boundary mobility, resulting in a strange low grain growth rate at up to an initial long annealing time.

ACKNOWLEDGMENTS

The authors acknowledge the National Nature Science Foundation of China, Grant Nos. 51171040 and 50771028, and the High Technology Research and Development Program of China (863), Grant No. 2013AAJY3164, for the financial support of this study.

REFERENCES

1. R.W. Siegel and G.E. Fougere: *Nanostruct. Mater.*, 1995, vol. 6 (1–4), pp. 205–16.
2. K. Youssef, R. Scattergood, K. Murty, and C. Koch: *Scripta Mater.*, 2006, vol. 54 (2), pp. 251–56.
3. K.V. Rajulapati, R.O. Scattergood, K.L. Murty, Z. Horita, T.G. Langdon, and C.C. Koch: *Metall. Mater. Trans. A*, 2008, vol. 39A, pp. 2528–34.
4. A.P. Garcia, D. Sen, and M.J. Buehler: *Metall. Mater. Trans. A*, 2011, vol. 42A, pp. 3889–97.
5. R. Phillips: *Curr. Opin. Solid State Mater. Sci.*, 1998, vol. 3 (6), pp. 526–32.
6. M. Založnik and H. Combeau: *Comput. Mater. Sci.*, 2010, vol. 48 (1), pp. 1–10.
7. W. Cai, V.V. Bulatov, J. Chang, J. Li, and S. Yip: *Phys. Rev. Lett.*, 2001, vol. 86 (25), pp. 5727–30.
8. Y.P. Zong, W. Guo, G. Wang, and F. Zhang: *J. Guangdong Non-Ferrous Met.*, 2005, vol. 15 (2), pp. 117–23.
9. E.B. Tadmor, M. Ortiz, and R. Phillips: *Phil. Mag. A*, 1996, vol. 73 (6), pp. 1529–63.
10. V. Vaithyanathan, C. Wolverton, and L.Q. Chen: *Phys. Rev. Lett.*, 2002, vol. 88 (12), p. 125503.
11. P. Hohenberg and W. Kohn: *Phys. Rev.*, 1964, vol. 136 (3B), pp. B864–B871.
12. B.J. Alder and T. Wainwright: *J. Chem. Phys.*, 1959, vol. 31, pp. 459–66.
13. N. Metropolis, A.W. Rosenbluth, M.N. Rosenbluth, A.H. Teller, and E. Teller: *J. Chem. Phys.*, 1953, vol. 21, pp. 1087–92.
14. H. Frost, C. Thompson, and D. Walton: *Acta Metall. Mater.*, 1990, vol. 38 (8), pp. 1455–62.
15. Z.S. Yu, P. Liu, and Y.Q. Long: *Mater. Heat Treat.*, 2008, vol. 37, pp. 94–98.
16. A. Karma and W.J. Rappel: *Phys. Rev. E*, 1996, vol. 53 (4), pp. 3017–20.
17. A. Karma and W.J. Rappel: *Phys. Rev. E*, 1998, vol. 57 (4), pp. 4323–49.
18. Y.U. Wang, Y.M. Jin, A.M. Cuitino, and A.G. Khachaturyan: *Acta Mater.*, 2001, vol. 49 (10), pp. 1847–57.
19. Y. Wen, B. Wang, J. Simmons, and Y. Wang: *Acta Mater.*, 2006, vol. 54 (8), pp. 2087–99.

20. B. Böttger, J. Eiken, M. Ohno, G. Klaus, M. Fehlbier, R. Schmid Fetzer, I. Steinbach, and A. Bührig Polaczek: *Adv. Eng. Mater.*, 2006, vol. 8 (4), pp. 241–47.
21. B. Böttger, J. Eiken, and I. Steinbach: *Acta Mater.*, 2006, vol. 54 (10), pp. 2697–2704.
22. Y.P. Zong, M.T. Wang, and W. Guo: *Acta Phys. Sin.-Chin. Ed.*, 2009, vol. 58, pp. S161–S168.
23. M. Wang, B.Y. Zong, and G. Wang: *Comput. Mater. Sci.*, 2009, vol. 45 (2), pp. 217–22.
24. X.G. Zhang, Y.P. Zong, M.T. Wang, and Y. Wu: *Acta Phys. Sin.-Chin. Ed.*, 2011, vol. 60 (6), pp. 755–63.
25. Y. Wu, B. Zong, and M. Wang: *Mater. Sci. Forum*, 2010, vol. 633, pp. 697–705.
26. X.G. Zhang, Y.P. Zong, and Y. Wu: *Acta Phys. Sin.-Chin. Ed.*, 2012, vol. 21 (8), pp. 088104-1–088104-9.
27. S.M. Allen and J.W. Cahn: *Acta Metall.*, 1979, vol. 27 (6), pp. 1085–95.
28. J.W. Cahn and J.E. Hilliard: *J. Chem. Phys.*, 1958, vol. 28 (2), pp. 258–67.
29. D. Fan and L.Q. Chen: *Acta Mater.*, 1997, vol. 45, pp. 611–22.
30. A. Kazaryan, Y. Wang, S. Dregia, and B.R. Patton: *Phys. Rev. B*, 2001, vol. 63 (18), pp. 184102-1–184102-11.
31. Y. Wen, J. Simmons, C. Shen, C. Woodward, and Y. Wang: *Acta Mater.*, 2003, vol. 51 (4), pp. 1123–32.
32. S.G. Kim, D.I. Kim, W.T. Kim, and Y.B. Park: *Phys. Rev. E*, 2006, vol. 74 (6), p. 061605.
33. Q. Chen, N. Ma, K. Wu, and Y. Wang: *Scripta Mater.*, 2004, vol. 50 (4), pp. 471–76.
34. C. Shen, Q. Chen, Y. Wen, J. Simmons, and Y. Wang: *Scripta Mater.*, 2004, vol. 50 (7), pp. 1023–28 and pp. 1029–34.
35. S.G. Kim, W.T. Kim, and T. Suzuki: *Phys. Rev. E*, 1998, vol. 58 (3), pp. 3316–22.
36. S.G. Kim, W.T. Kim, and T. Suzuki: *Phys. Rev. E*, 1999, vol. 60 (6), pp. 7186–97.
37. T. Nishizawa and S.M. Hao: *Thermodynamics of Microstructure*, 1st ed., Chemical Industry Press, Beijing, 2006, pp. 135–136.
38. C. Shek, J. Lai, and G. Lin: *Nanostruct. Mater.*, 1999, vol. 11 (7), pp. 887–93.
39. J.Q. Wang, P. Geng, M.G. Zeng, B.J. Zhang, and C.F. Qian: *Chin. J. Mater. Res.*, 1997, vol. 11, pp. 316–18.
40. Y. Zhang, N. Tao, and K. Lu: *Acta Mater.*, 2008, vol. 56 (11), pp. 2429–40.
41. C. Deng: *Fabrication of Ultra-Fine Grain Magnesium Alloy by Powder Metallurgy and Research on the Microstructure and Property*, Harbin Institute of Technology, Harbin, 2009, p. 24.
42. M. Hillert: *Acta Metall.*, 1965, vol. 13 (3), pp. 227–38.
43. R.C. Liu, L.Y. Wang, L.G. Gu, and G.S. Huang: *Light Alloy Fabric Technol.*, 2004, vol. 32, pp. 22–25.
44. T. Malow and C. Koch: *Acta Mater.*, 1997, vol. 45 (5), pp. 2177–86.
45. B. Färber, E. Cadel, A. Menand, G. Schmitz, and R. Kirchheim: *Acta Mater.*, 2000, vol. 48 (3), pp. 789–96.
46. H. Gleiter: *Progr. Mater. Sci.*, 1989, vol. 33, pp. 223–315.
47. A. Michels, C. Krill, H. Ehrhardt, R. Birringer, and D. Wu: *Acta Mater.*, 1999, vol. 47 (7), pp. 2143–52.